Experimental realization of quantum non-Markovianity through the convex mixing of Pauli semigroups on an NMR quantum processor

Vaishali Gulati,[1,*] Vinayak Jagadish,[2,3,†] R. Srikanth,[4,‡] and Kavita Dorai[1,§]

[1]*Department of Physical Sciences, Indian Institute of Science Education & Research Mohali, Sector 81 SAS Nagar, Manauli PO 140306 Punjab, India*

[2]*Instytut Fizyki Teoretycznej, Uniwersytet Jagielloński, Łojasiewicza 11, 30-348 Kraków, Poland*

[3]*QTF Centre of Excellence, Department of Physics, University of Helsinki, P.O. Box 43, FI-00014 Helsinki, Finland*

[4]*Theoretical Sciences Division, Poornaprajna Institute of Scientific Research (PPISR), Bidalur post, Devanahalli, Bengaluru 562164, India*

(Received 7 July 2023; revised 28 March 2024; accepted 5 April 2024; published 19 April 2024)

This experimental study aims to investigate the convex combinations of Pauli semigroups with arbitrary mixing parameters to determine whether the resulting dynamical map exhibits Markovian or non-Markovian behavior. Specifically, we consider the cases of equal as well as unequal mixing of two Pauli semigroups, and demonstrate that the resulting map is always non-Markovian. Additionally, we study three cases of three-way mixing of the three Pauli semigroups and determine the Markovianity or non-Markovianity of the resulting maps by experimentally determining the decay rates. To simulate the nonunitary dynamics of a single-qubit system with different mixing combinations of Pauli semigroups on an NMR quantum processor, we use an algorithm involving two ancillary qubits. The experimental results align with the theoretical predictions.

DOI: 10.1103/PhysRevA.109.042419

I. INTRODUCTION

The field of quantum computing is rapidly developing, and there is a crucial need to develop reliable methods to characterize and control quantum systems. Quantum systems can interact with their environment in various ways, leading to decoherence and dissipation, which could have a deleterious effect on the computational protocols. The study of open quantum systems [1,2] therefore has significant implications for applications in quantum information processing, quantum computing, and quantum communication. Recent research has focused on the effect of decoherence on the performance of quantum computers [3] and the use of error correction codes to address this issue [4]. A critical aspect of open quantum systems is characterizing their dynamical behavior, with a particular focus on the distinction between Markovian and non-Markovian dynamics [5–7]. The theory of non-Markovian dynamics has become an important area of research, with a focus on characterization, quantification, and detection of non-Markovian behavior [8–10].

The reduced dynamics of the quantum system of interest undergoing open evolution is described by a time-continuous family of completely positive (CP) and trace-preserving (TP) linear maps $\{\Lambda(t) : t \geqslant 0, \Lambda(0) = \mathbb{1}\}$ known as the quantum dynamical map, acting on the bounded operators of the Hilbert space of the system of interest [11,12]. The dynamical map is also related to the time-local generator $\mathcal{L}(t)$ [13] in the time-local master equation, $\dot{\Lambda}(t) = \mathcal{L}(t)\Lambda(t)$, with

$$\mathcal{L}(t)[\rho] = -\imath[H(t), \rho] + \sum_i \gamma_i(t)\left[L_i(t)\rho L_i(t)^\dagger - \frac{1}{2}\{L_i(t)^\dagger L_i(t), \rho\}\right], \tag{1}$$

where $H(t)$ is the effective Hamiltonian, $L_i(t)$ the noise operators, and $\gamma_i(t)$ the decoherence rates. The divisibility of the dynamical map is expressed as follows:

$$\Lambda(t_f, t_i) = V(t_f, t)\Lambda(t, t_i), \quad \forall t_f \geqslant t \geqslant t_i \geqslant 0. \tag{2}$$

The map is CP divisible if for all t, the propagator $V(t_f, t)$ is CP and the corresponding decay rates $\gamma_i(t)$ are positive at all times. Otherwise, the map is said to be CP indivisible.

In contrast with classical non-Markovianity, quantum non-Markovianity does not have a unique definition [5,6,14]. Two major proposals to address quantum non-Markovianity are based on the CP-indivisibility criterion (RHP) [15,16] and on the distinguishability of states (BLP) [17,18]. According to the RHP divisibility criterion [15], a quantum dynamical map is non-Markovian if it is CP indivisible. A Markovian evolution, therefore, is CP divisible, with all the decay rates $\gamma_i(t)$ in the time-local master equation (1) are positive at all times. A temporarily negative decay rate is therefore a signature of CP indivisibility of the map and therefore non-Markovianity. According to the BLP definition [17], a quantum dynamical map $\Lambda(t)$ is said to be Markovian if it does not increase the distinguishability of two initial states ρ_1 and ρ_2, i.e., if $\|\Lambda(t)(\rho_1) - \Lambda(t)(\rho_2)\| \leqslant \|\Lambda(0)(\rho_1) - \Lambda(0)(\rho_2)\|$, where $\|\cdot\|$ denotes the trace distance. In this work, we stick to the CP-indivisibility criterion of non-Markovianity.

*vaishali@iisermohali.ac.in
†vinayak.jagadish@helsinki.fi
‡srik@poornaprajna.org
§kavita@iisermohali.ac.in

Convex combinations of Pauli semigroups and time-dependent Markovian Pauli dynamical maps were studied in Refs. [19,20] discussing the geometrical aspects and non-Markovianity. These results showed the nonconvexity of the sets of CP-divisible and CP-indivisible Pauli dynamical maps. Convex combinations of semigroups of generalized Pauli dynamical maps have been addressed in Ref. [21]. In Ref. [22], it was shown that an eternally non-Markovian evolution arises from a mixture of Markovian semigroups. Convex combinations of noninvertible dynamical maps have also been studied recently [23–26]. For the case of generalized Pauli dynamical maps, it was shown that mixing invertible maps can never result in noninvertible maps [23]. Subsequently, it was also shown that noninvertibility of the generalized Pauli input maps is necessary for getting a semigroup [24]. The fraction of (non)invertible maps obtained by mixing noninvertible generalized Pauli maps was quantified in Ref. [25]. The measure of the set of non-Markovian maps obtained by mixing noninvertible Pauli maps was studied in Ref. [26].

In recent years, there has been a growing interest in the experimental implementation of non-Markovian dynamics in various physical systems, including quantum dots [27–29], superconducting qubits [30], trapped ions [31,32], and NMR systems [33,34]. NMR systems, in particular, are a useful platform to investigate non-Markovian dynamics due to their excellent ability to control and manipulate system-environment interactions. Various studies in NMR investigate different quantum correlations present in the system [35,36] and their dynamics under various environments [37,38].

In this work, we aim to experimentally study the behavior of a single-qubit system under the effect of different mixing combinations of Pauli semigroups on an NMR quantum processor. We demonstrate that the mixing of any two Markovian Pauli semigroups produces a map which is CP indivisible and therefore RHP non-Markovian. One of the decay rates always turns out to be negative in this scenario. We also verify our experimental results for arbitrary choices of the mixing parameters for the dynamical semigroup realizations of the three Pauli semigroups which are in agreement with the notion of Pauli simplex as defined in Ref. [19]. We note that the non-Markovian nature of the map becomes apparent when one or more of the decay rates becomes negative. We consider the case of a single qubit with two ancilla qubits to simulate nonunitary dynamics and make use of the algorithm for the circuit design as in Ref. [39].

The rest of this paper is organized as follows. Section II briefly describes the theory of the convex combinations of Pauli semigroups. The experimental details and results are presented in Sec. III. We then conclude in Sec. IV.

II. CONVEX COMBINATION OF PAULI SEMIGROUPS

Consider the three Pauli dynamical semigroups,

$$\Lambda_i(t)[\rho] = [1 - p(t)]\rho + p(t)\sigma_i\rho\sigma_i, \quad i = 1, 2, 3, \quad \text{with}$$
$$p(t) = \frac{1 - e^{-ct}}{2}, \quad c > 0. \tag{3}$$

Here, $p(t)$ is the decoherence function and σ_i are the Pauli matrices.

The convex combination of the three Pauli semigroups Eq. (3), each mixed in proportions of x_i, is

$$\tilde{\Lambda}(t) = \sum_{i=1}^{3} x_i\Lambda_i(t), \quad \left(x_i > 0, \sum_i x_i = 1\right). \tag{4}$$

Let us call the three $\Lambda_i(t)$ input maps and $\tilde{\Lambda}(t)$ the output map. The associated time-local master equation for $\tilde{\Lambda}(t)$ is

$$\mathcal{L}(t)[\rho] = \sum_{i=1}^{3} \gamma_i(t)(\sigma_i\rho\sigma_i - \rho), \tag{5}$$

with the decay rates

$$\begin{aligned}
\gamma_1(t) &= \left(\frac{1-x_2}{1-2(1-x_2)p(t)} + \frac{1-x_3}{1-2(1-x_3)p(t)} - \frac{1-x_1}{1-2(1-x_1)p(t)}\right)\frac{\dot{p}(t)}{2} \\
\gamma_2(t) &= \left(\frac{1-x_1}{1-2(1-x_1)p(t)} + \frac{1-x_3}{1-2(1-x_3)p(t)} - \frac{1-x_2}{1-2(1-x_2)p(t)}\right)\frac{\dot{p}(t)}{2} \\
\gamma_3(t) &= \left(\frac{1-x_1}{1-2(1-x_1)p(t)} + \frac{1-x_2}{1-2(1-x_2)p(t)} - \frac{1-x_3}{1-2(1-x_3)p(t)}\right)\frac{\dot{p}(t)}{2}.
\end{aligned} \tag{6}$$

The CP divisibility and, therefore, the Markovianity of output map $\tilde{\Lambda}(t)$ depends on the mixing coefficients x_i. For instance, an equal mixing of the three Pauli semigroups results in a Markovian output. The fraction of non-Markovian (CP-indivisible) maps obtained by mixing Pauli semigroups was reported in Ref. [19]. As opposed to three-way mixing, any mixing of two Pauli semigroups is always non-Markovian. To this end, let $x_1 = 0$. The decay rate $\gamma_1(t)$ turns out to be

$$\gamma_1(t) = -\left[\frac{(1-x_2)x_2[1-p(t)]p(t)}{[1-2p(t)][1-2(1-x_2)p(t)][1-2x_2p(t)]}\right]\dot{p}(t), \tag{7}$$

which remains negative for all values of x_2. (Note that $x_3 = 1 - x_2$.)

III. EXPERIMENTAL ANALYSIS OF MARKOVIANITY AND NON-MARKOVIANITY

A. NMR simulation of Pauli semigroups

A dynamical map acting on a system of d-dimensional Hilbert space could be simulated by a d^2-dimensional ancilla if one allows the most general unitary evolution of the total system under the assumption that the ancilla is initialized in a pure state [40]. Therefore, to simulate maps on a qubit, a two-qubit ancilla is sufficient. The finite time map $\tilde{\Lambda}(t)$ as in

Eq. (4) being CP and TP admits an operator-sum representation, $\tilde{\Lambda}(t)(\rho) = \sum_k E_k(t)\rho E_k^\dagger(t)$, where the operator $E_k(t)$ satisfies the trace-preservation condition, $\sum_k E_k^\dagger(t)E_k(t) = \mathbb{1}$.

The nonunitary operator $E_k(t)$ associated with the dynamical map can be decomposed into a linear combination of four unitary operators (Pauli matrices σ_i in this case) and are experimentally implemented using two ancillary qubits added to the working system. Efficient implementation of the nonunitary transformation represented by $\tilde{\Lambda}(t)$ is achievable when suitable unitary operations U, V, and W are found, such that $E_k = \sum_i W_{ki}V_{i0}U_i$. By applying the overall unitary operation $(I \otimes W)U(I \otimes V)$ to the initial state of the working system and ancillary system, followed by the trace-out of the ancilla, the simulation of the map is obtained. The algorithm involving three unitaries offers the advantage in implementing the maps involving the convex mixtures of Pauli semigroups in a more general manner. This approach eliminates the need to design separate circuits for each specific mixing combination. By incorporating three unitaries into the algorithm, it becomes possible to dynamically adjust and experiment with different mixing parameters and Pauli operators, allowing for greater flexibility and versatility in simulating the desired nonunitary dynamics. The algorithm is as follows.

(1) Transforming the state of the ancilla qubits: After initializing the three-qubit system in the state $|0\rangle_s|00\rangle$, where $|0\rangle_s$ is the state of the system qubit and $|00\rangle$ that of the ancillary qubits, a unitary operation V is performed on the ancillary qubits. The composite state evolves to $V_{00}|0\rangle_s|00\rangle + V_{10}|0\rangle_s|01\rangle + V_{20}|0\rangle_s|10\rangle + V_{30}|0\rangle_s|11\rangle$. The mixing parameters and the decoherence function associated with the Kraus operators determine the values in the first column of the unitary matrix V.

(2) Transforming the state of the system: The unitary operations σ_i are applied on the system qubit depending on the state of the ancilla qubits acting as control qubits:

$$U = \sigma_0 \otimes |00\rangle\langle 00| + \sigma_1 \otimes |01\rangle\langle 01| + \sigma_2 \otimes |10\rangle\langle 10| + \sigma_3 \otimes |11\rangle\langle 11|, \tag{8}$$

where σ_0 is the identity matrix. The system now evolves to the state $V_{00}\sigma_0|0\rangle_s|00\rangle + V_{10}\sigma_1|0\rangle_s|01\rangle + V_{20}\sigma_2|0\rangle_s|10\rangle + V_{30}\sigma_3|0\rangle_s|11\rangle$.

(3) Finally, the unitary operation W is performed on the ancillary system, which transforms the state into $\sum_{i,k=0}^{3} W_{ki}V_{i0}\sigma_i|0\rangle_s|k\rangle$, where $E_k = \sum_{i=0}^{3} W_{ki}V_{i0}\sigma_i$. The elements of matrix W are uniquely determined by the choice of matrix elements of V. We obtain the W matrix as the identity matrix in our cases.

(4) On measuring the final state of the working system with the ancillary system in the state $|k\rangle\langle k|$, we obtain $E_k|0\rangle_s\langle 0|_s E_k^\dagger$. By tracing out the ancillary qubits, summing over each state $|k\rangle\langle k|$, the result is $\sum_k E_k(t)|0\rangle_s\langle 0|_s E_k^\dagger(t)$, which corresponds to simulating the map $\tilde{\Lambda}(\rho)$ where the initial state of the system ρ is $|0\rangle\langle 0|$.

The specific forms of the matrices V used in the experiments depend on the dynamical map under consideration, and the specific forms used in our experiments are given in the following section.

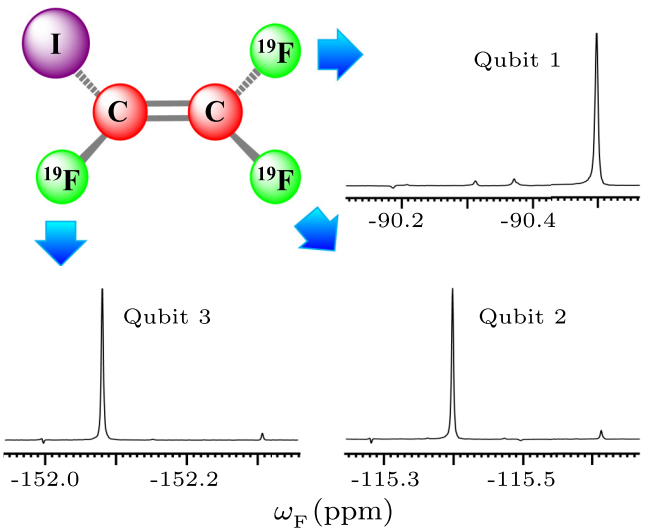

FIG. 1. The structure of the molecule trifluoroiodoethylene with three NMR active spin $-1/2$ ^{19}F nuclei acting as three qubits, along with the NMR spectra of the pseudopure state $|000\rangle$ which represents the initial state of the three-qubit system. The x axis represents the frequency scale presented in parts per million (ppm). The negative values on the x axis represent the frequency offset from the reference frequency (indicating upfield shifts for ^{19}F nuclei).

B. Experimental parameters

The three NMR qubits were realized using the three ^{19}F spin-1/2 nuclei in the molecule trifluoroiodoethylene (Fig. 1) dissolved in the deuterated solvent, d6-acetone. All experiments were performed at ambient temperature (∼298 K) on a Bruker AVANCE-III 400 MHz NMR spectrometer equipped with a broadband observe (BBO) probe. The high-temperature, high-field approximation simplifies the NMR Hamiltonian by neglecting certain terms when the thermal and Zeeman energies dominate over other interactions. This approximation enables easier analysis and calculations in NMR experiments. The resulting Hamiltonian, assuming weak scalar coupling J_{ij} between spins i and j, is given by [41]

$$\mathcal{H} = -\sum_{i=1}^{3} \omega_i I_{iz} + 2\pi \sum_{i<j}^{3} J_{ij} I_{iz} I_{jz}, \tag{9}$$

where ω_i is the chemical shift of the ith spin, and I_{iz} represents the z component of the spin-$\frac{1}{2}$ operator for the ith spin.

Nuclear spins at thermal equilibrium are represented by the density operator,

$$\rho = \frac{\exp(-H/k_B T)}{Z}, \tag{10}$$

where H is the Hamiltonian of the system, k_B is the Boltzmann constant, T is the temperature, and Z is the partition function.

Starting from thermal equilibrium, the system is prepared in a pseudopure state (PPS) using the spatial averaging technique [42,43], with the density matrix corresponding to the PPS being given by

$$\rho_{000} = \frac{(1-\epsilon)}{8}\mathbb{1}_8 + \epsilon|000\rangle\langle 000|, \tag{11}$$

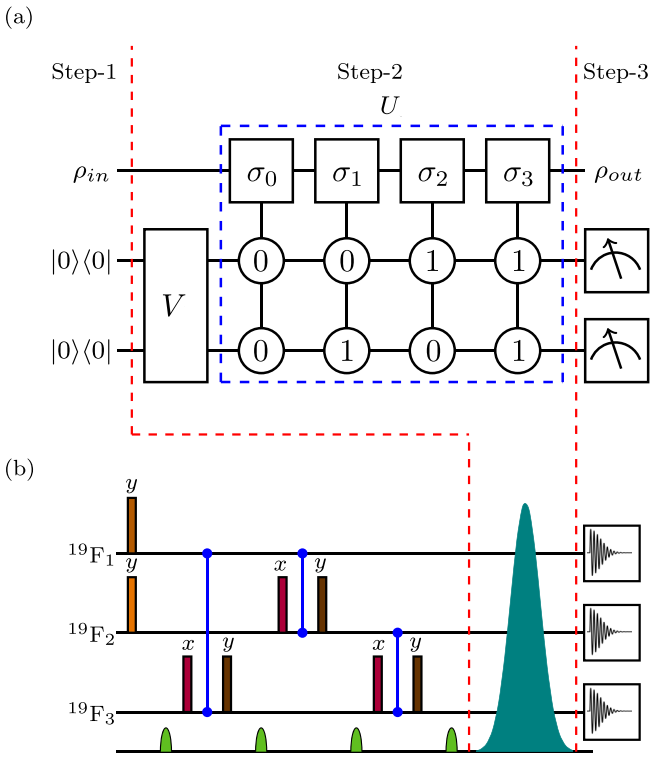

FIG. 2. (a) Schematic of the circuit used to simulate the dynamical map obtained from the convex combination of two and three Pauli dynamical maps. For both two- and three-dynamical-map mixing, the controlled operation U is the same. σ_i denote the Pauli matrices, with σ_0 being the identity matrix. The unitary operation V is different for the cases of two-way and three-way mixing. The W operation is equivalent to the identity operation and hence not implemented experimentally. (b) The NMR pulse sequence used to simulate the map. The rectangular shapes represent rf pulses of differing angles and phases (which are written on the top of each pulse). CNOT operations between two qubits are represented by blue lines between the corresponding qubits. Step 1 corresponds to the preparation of the input state. Gradient pulses are represented by shaped green curves, while the GRAPE-optimized pulse to implement Step 2 of the circuit is represented by a large dark green curve, applied simultaneously on all three qubits. Step 3 corresponds to measurements on all three qubits.

where $\epsilon \sim 10^{-5}$ is the spin polarization at room temperature and $\mathbb{1}_8$ is the 8×8 identity operator. The identity part of the density operator plays no role and the NMR signal arises solely from the traceless part of the density matrix given in Eq. (11).

T_1 and T_2 relaxation times in NMR describe the return to equilibrium and loss of phase coherence of nuclear spins. T_1 measures the recovery of longitudinal magnetization, while T_2 measures the decay of transverse magnetization. However, the faster decay of transverse magnetization observed in practice is often attributed to T_2^* relaxation, which combines intrinsic T_2 relaxation and magnetic field variation effects. T_2^* for our experimental setup yields a value of approximately 0.1869 s. The experimentally measured scalar couplings are given by $J_{12} = 69.65$ Hz, $J_{13} = 47.67$ Hz, and $J_{23} = -128.32$ Hz.

The rf required for creating the PPS state was designed using the gradient ascent pulse engineering (GRAPE) [44] technique, along with pulsed magnetic field gradients [45]. The GRAPE pulses obtained are for the collective operation of U and V at each time point. To clarify, for each time point, a specific unitary matrix is obtained by the product of U and V. The GRAPE pulse length varies according to different unitaries simulated at different time points. For instance, at $t = 0.1$ s, the GRAPE pulse length is approximately 700 μs, and at $t = 1.5$ s, it is approximately 2500 μs. The system was evolved from the PPS to the other states via state-to-state transfer unitaries, and all states were created with high fidelities $\geqslant 0.99$. The standard methods for quantum state reconstruction for NMR quantum information processing typically involve performing full state tomography [46,47] which is computationally expensive, although some alternatives involving maximum likelihood estimation have been proposed and used [48]. For this work, we used a least squares constrained convex optimization method to reconstruct the density matrix of the desired state [49,50]. Fidelities of the experimentally reconstructed states (as compared to the theoretically expected state) were computed using the measure [51,52]

$$\mathcal{F}(\chi_{\text{expt}}, \chi_{\text{theo}}) = \frac{|\text{Tr}[\chi_{\text{expt}}\chi_{\text{theo}}^{\dagger}]|}{\sqrt{\text{Tr}[\chi_{\text{expt}}^{\dagger}\chi_{\text{expt}}]\text{Tr}[\chi_{\text{theo}}^{\dagger}\chi_{\text{theo}}]}}, \tag{12}$$

where χ_{theo} and χ_{expt} denote the theoretical and experimental density matrices, respectively. We experimentally prepared the PPS with a fidelity of 0.9979 ± 0.0001. The PPS fidelity without convex optimization, calculated using the linear inversion method, is 0.9933 ± 0.0005.

1. Mixing of two Pauli semigroups

We experimentally demonstrate mixing of two Pauli semigroups for two cases each with the decoherence parameter $p(t) = [1 - \exp(-2t)]/2$. To this end, we consider convex mixing as

$$\tilde{\Lambda}(t)(\rho) = a\Lambda_3(t)(\rho) + (1-a)\Lambda_2(t)(\rho). \tag{13}$$

The two cases considered are (1) equal mixing with the mixing parameter $a = 0.5$ and (2) unequal mixing with the mixing parameter $a = 0.25$.

For the simulation of mixing two Pauli semigroups, the algorithm described above leads to the following matrix:

$$V = \begin{pmatrix} \sqrt{1-p(t)} & \sqrt{p(t)} & 0 & 0 \\ 0 & 0 & 1 & 0 \\ \sqrt{p(t)(1-a)} & -\sqrt{(1-a)[1-p(t)]} & 0 & \sqrt{a} \\ \sqrt{ap(t)} & -\sqrt{a[1-p(t)]} & 0 & -\sqrt{1-a} \end{pmatrix}. \tag{14}$$

To implement the unitary for the convex combination of the case of mixing two and three Pauli semigroups experimentally, we utilized the quantum circuit shown in Fig. 2. For mixing of both two and three semigroups, the controlled operation U is the same, as in Eq. (8). The unitary operation V is different for the two-way and three-way mixing. The W operation is equivalent to the identity operation for both cases and is hence not implemented experimentally. For the implementation of the NMR pulse sequence, GRAPE-optimized pulses are used. The unitaries U and V are designed so as to be implemented by use of a single pulse for each time point in all the cases. The experimental procedure involves three steps:

(1) Initialization: The system is prepared in the state $|000\rangle\langle 000|$ with the help of optimized pulses and magnetic field gradients.

(2) Simulation of the nonunitary dynamics: The implementation of U and V with GRAPE optimized pulses.

(3) Measurement: The acquisition and tomography pulses are applied.

The rectangular shapes in Fig. 2 depict the rf pulses used to prepare the initial pseudopure state required for Step 1 of the algorithm. Each rectangle is associated with specific phases, which are indicated above them. The magnetic field direction is assumed to align with the z axis. The rf pulses are applied along the x or y axis at specific angles, allowing precise control over qubit rotations and transformations. With the knowledge of the desired phases and angles of the rf pulses, we can perform operations like single-qubit rotations and two-qubit gates. For example, the first qubit is rotated by an angle of $\theta_1 = \frac{5\pi}{12}$ radians around the y axis, while the second qubit is rotated by an angle of $\theta_2 = \frac{\pi}{3}$ radians. CNOT operations between two qubits are represented by blue lines between the corresponding qubits. The complete pulse sequence corresponding to the CNOT gate can be found in Ref. [35]. Before the CNOT gate operation, an x pulse with an angle of $\frac{\pi}{4}$ is applied. This pulse rotates the state of the qubit around the x axis. Following the CNOT gate, a y pulse with an angle of $-\frac{\pi}{4}$ is applied, which rotates the state around the y axis. The angles and pulses of the rf pulses or gate operations are carefully chosen to achieve the desired output state or perform the targeted operation. The specific choice of angles or gates depend on our goal which in this case is to prepare the PPS. After the initialization, a GRAPE pulse corresponding to Step 2 of the algorithm is applied. This pulse applies the unitary operations V and U, depending on the specific case being considered.

2. Mixing of three Pauli semigroups

We next consider the case of the convex combination of three Pauli semigroups. We experimentally demonstrate this for three cases, each with the decoherence parameter $p(t) = [1 - \exp(-3t)]/2$:

(1) equal mixing with mixing parameters $x_1 = x_2 = x_3 = 0.33$,

(2) unequal mixing with mixing parameters $x_1 = x_3 = 0.3, x_2 = 0.4$, and

(3) unequal mixing with mixing parameters $x_1 = 0.2, x_2 = x_3 = 0.4$.

The V matrix in this case is evaluated to be

$$V = \begin{pmatrix} \sqrt{1-p(t)} & \sqrt{p(t)} & 0 & 0 \\ \sqrt{x_1 p(t)} & -\sqrt{x_1[1-p(t)]} & \sqrt{1-x_1} & 0 \\ \sqrt{x_2 p(t)} & -\sqrt{x_2[1-p(t)]} & -\sqrt{\frac{x_1 x_2}{1-x_1}} & \sqrt{\frac{x_3}{1-x_1}} \\ \sqrt{x_3 p(t)} & -\sqrt{x_3[1-p(t)]} & -\sqrt{\frac{x_1 x_3}{1-x_1}} & -\frac{x_2}{\sqrt{x_2(1-x_1)}} \end{pmatrix}. \tag{15}$$

The decay rate of the decoherence parameter $p(t)$ is dependent on the chosen constant c. Therefore, determining the optimal time interval required to study the behavior of the system is directly linked to the selection of c. Shorter time periods are preferable to minimize decoherence during experimental duration. The appropriate choice of c is crucial to effectively study the impact of the resulting dynamical map on the system, while minimizing noise interference.

The final three-qubit density matrix was reconstructed using the least squares constrained convex optimization method. The average fidelity of the experimental matrices obtained is 0.98 ± 0.01. The experimental output matrix for the single-qubit system is obtained after tracing over the ancilla qubits. We plot bar graphs (Fig. 3) to visually compare the real and imaginary parts of the theoretical and experimental density matrices for the specific example of the second case of mixing two semigroups at $t = 0.1$ ms. The fidelity of the experimental state, in this case, is 0.99. The decoherence parameter $p(t)$ is computed at every time point from the output matrix and the experimental data is fitted to obtain the experimental parameter $p_e(t)$ and its time evolution $\dot{p}_e(t)$. The experimental decay rates are subsequently computed with the help of Eq. (6).

Figures 4 and 5 depict a comparison of the theoretical and experimental results for the two-way mixing case, for equal and unequal mixing, respectively. For each case, the decoherence parameter $p(t)$ is plotted in the top panel. The blue dots represent the experimental data with error bars, the blue curves represent the experimental fits, and the red dashed curves represent the theoretical parameters. The decay rates obtained from the experimental data $\gamma_1(t)$ are negative for both case (1) and case (2), indicating that the resultant dynamical map, when two Pauli semigroups maps are mixed, is non-Markovian, which is consistent with Theorem 1 in Ref. [19].

Figures 6–8 present a comparison of the theoretical and experimental results for the case of three-way mixing. For each case, the decoherence parameter $p(t)$ is plotted in the top panel. The blue dots represent the experimental data with error bars, the blue curves represent the experimental fits, and the red dashed curves represent the theoretical parameters. To

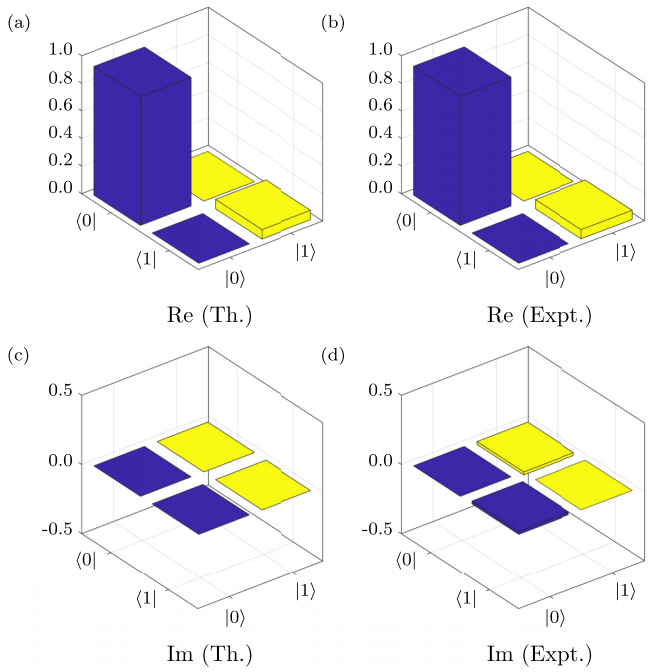

FIG. 3. Bar plots illustrating the real (Re) and imaginary (Im) components of the theoretical (Th.) and experimental (Expt.) density matrices for the specific case of unequal mixing of two Pauli semigroups at $t = 0.1$ ms.

determine whether the resultant dynamical map is Markovian or non-Markovian, the decay rates are analyzed. The decay rates $\gamma_1(t)$, $\gamma_2(t)$, $\gamma_3(t)$ were all positive for case (1) and case (2) as shown in plots (b), (c), and (d) respectively, indicating that the resultant dynamical maps are Markovian. However, for case (3), the negative decay rate of $\gamma_1(t)$ suggests that the resultant dynamical map is non-Markovian, which is consistent with the theoretical results.

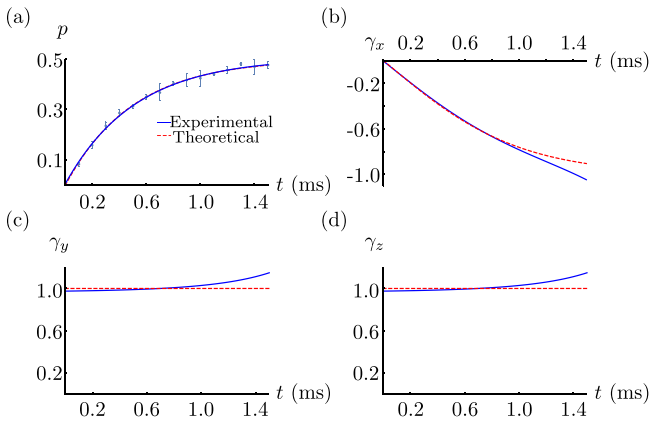

FIG. 4. Convex combination of two Pauli semigroups for the case of equal mixing. (a) Comparison of the theoretical and experimental decoherence parameters $p(t)$. (b) Comparison of theoretical and experimental decay rates $\gamma_1(t)$, $\gamma_2(t)$, $\gamma_3(t)$ with mixing parameter $a = 0.5$. The red dashed and blue curves represent the theoretical and the fit to the experimental parameters, respectively. Experimental data points with error bars are represented by blue dots. The decay rate $\gamma_1(t)$ is negative throughout, indicating non-Markovianity.

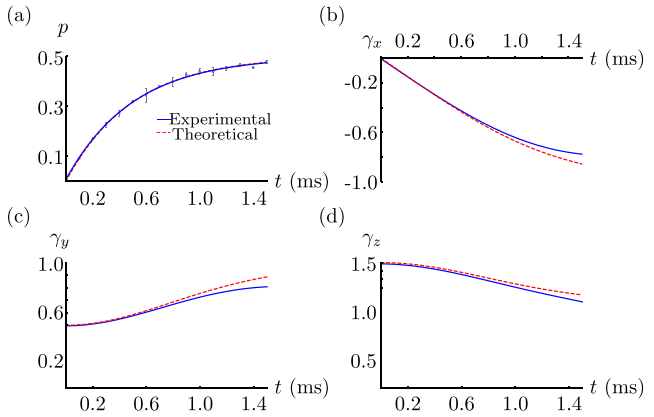

FIG. 5. Convex combination of two Pauli dynamical maps for the case of inequal mixing. (a) Comparison of the theoretical and experimental decoherence parameters $p(t)$. (b) Comparison of theoretical and experimental decay rates $\gamma_1(t)$, $\gamma_2(t)$, $\gamma_3(t)$ with mixing parameter $a = 0.25$. The red dashed and blue curves represent the theoretical and the fit to the experimental parameters, respectively. Experimental data points with error bars are represented by blue dots. The decay rate $\gamma_1(t)$ is negative throughout, indicating non-Markovianity.

Figures 4–8 provide clear evidence of the agreement between the theoretical and experimental results. The experimental results clearly corroborate the Markovian or non-Markovian nature of the dynamical map in cases of both two- and three-way mixing, which is consistent with Theorem 1 and the Pauli simplex in Ref. [19]. The outcomes presented here, which successfully demonstrate the effects of combining different Pauli semigroups with arbitrary mixing parameters, provide valuable insights for the study of memory effects in open quantum systems. Moreover, these results are significant

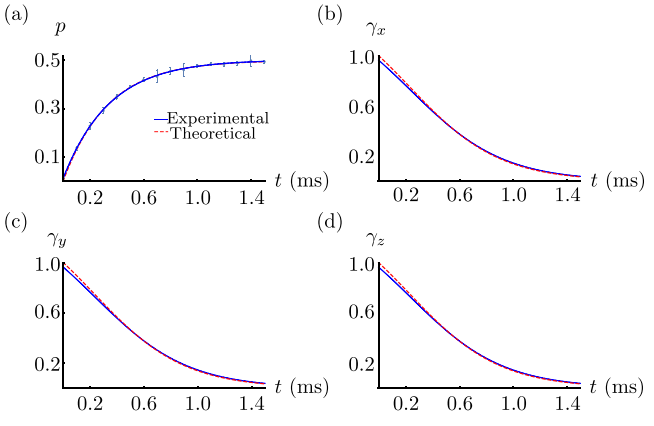

FIG. 6. Convex combination of three Pauli dynamical maps for the case of equal mixing. (a) Comparison of the theoretical and experimental decoherence parameters $p(t)$. (b) Comparison of theoretical and experimental decay rates $\gamma_1(t)$, $\gamma_2(t)$, $\gamma_3(t)$ with mixing parameters $x_1 = x_2 = x_3 = 0.33$. The red dashed and blue curves represent the theoretical and the fit to the experimental parameters, respectively. Experimental data points with error bars are represented by blue dots. All the decay rates are positive, indicating that the resulting map is Markovian.

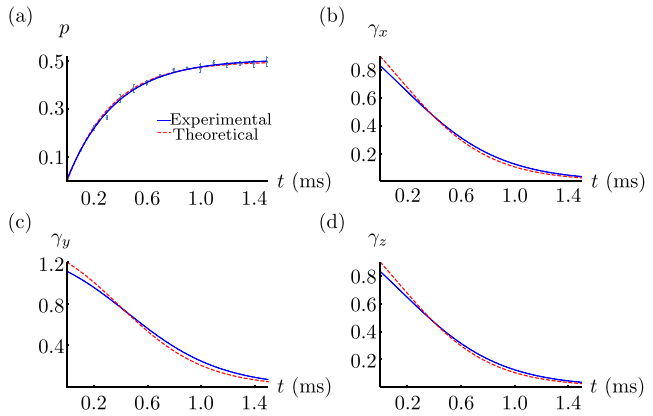

FIG. 7. Convex combination of three Pauli dynamical maps for the case of inequal mixing. (a) Comparison of the theoretical and experimental decoherence parameters $p(t)$. (b) Comparison of theoretical and experimental decay rates $\gamma_1(t)$, $\gamma_2(t)$, $\gamma_3(t)$ with mixing parameters $x_1 = x_3 = 0.3, x_2 = 0.4$, respectively. The red dashed and blue curves represent the theoretical and the fit to the experimental parameters, respectively. Experimental data points with error bars are represented by blue dots. All the decay rates are positive, indicating that the resulting map is Markovian.

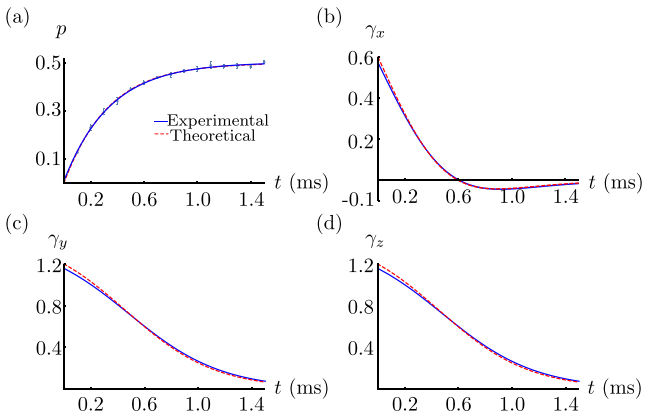

FIG. 8. Convex combination of three Pauli dynamical maps for the case of inequal mixing. (a) Comparison of the theoretical and experimental decoherence parameters $p(t)$. (b)–(d) Comparison of theoretical and experimental decay rates $\gamma_1(t)$, $\gamma_2(t)$, $\gamma_3(t)$ with mixing parameters $x_1 = 0.2$ and $x_2 = x_3 = 0.4$, respectively. The red dashed and blue curves represent the theoretical and the fit to the experimental parameters, respectively. Experimental data points with error bars are represented by blue dots. The negativity of the decay rate $\gamma_1(t)$ indicates non-Markovianity of the resulting map.

for the development of quantum error correction and fault-tolerant quantum computing.

IV. CONCLUSIONS

In our experimental study, we have successfully demonstrated the combination of two and three Pauli semigroups, with different mixing parameters. The main objective was to investigate the Markovianity and non-Markovianity of the resulting dynamical maps. By analyzing the decay rates associated with these dynamical maps, we were able to assess the characteristics of the quantum maps under investigation. We compared our experimental analysis with the theoretical predictions. The comparative analysis allowed us to validate the accuracy of our experimental findings and establish the reliability of our approach. The good agreement between the experimental results and theoretical expectations highlights the efficacy of our methodology in capturing the underlying dynamics of the system-environment interactions. This research represents a significant step forward in advancing our understanding of quantum correlations and the interplay between the system and its surrounding environment. Overall, our experimental investigation contributes to the growing body of knowledge in the field of quantum dynamics, paving the way for further studies on the characterization and manipulation of quantum information in realistic environments. NMR, with its precise control, long coherence times, and accurate measurements, serves as a good platform for simulating the dynamics of open quantum systems and understanding the correlations between quantum systems and their environment.

ACKNOWLEDGMENTS

V.J. acknowledges financial support by the Foundation for Polish Science through the TEAM-NET project (Contract No. POIR.04.04.00-00-17C1/18-00). R.S. and K.D. acknowledge financial support from Department of Science and Technology (DST), India, Grants No. DST/ICPS/QuST/Theme-1/2019/14 and No. DST/ICPS/QuST/Theme-2/2019/Q-74, respectively. R.S. also acknowledges the support of the Government of India DST/SERB Grant No. CRG/2022/008345.

[1] H.-P. Breuer and F. Petruccione, *The Theory of Open Quantum Systems* (Oxford University, New York, 2007)
[2] S. Haroche and J.-M. Raimond, *Exploring the Quantum: Atoms, Cavities, and Photons* (Oxford University, New York, 2006).
[3] E. Knill, Nature (London) **434**, 39 (2005).
[4] A. G. Fowler, M. Mariantoni, J. M. Martinis, and A. N. Cleland, Phys. Rev. A **86**, 032324 (2012).
[5] H.-P. Breuer, E.-M. Laine, J. Piilo, and B. Vacchini, Rev. Mod. Phys. **88**, 021002 (2016).
[6] L. Li, M. J. Hall, and H. M. Wiseman, Phys. Rep. **759**, 1 (2018).
[7] I. de Vega and D. Alonso, Rev. Mod. Phys. **89**, 015001 (2017).
[8] A. Carmele and S. Reitzenstein, Nanophotonics **8**, 655 (2019).
[9] L. Zhang, H. Liang, Y. Sun, and C. K. Ahn, IEEE Trans. Syst. Man Cybern, Syst. **51**, 2370 (2021).
[10] M. Jiang and S. Luo, Phys. Rev. A **88**, 034101 (2013).
[11] E. C. G. Sudarshan, P. M. Mathews, and J. Rau, Phys. Rev. **121**, 920 (1961).
[12] V. Jagadish and F. Petruccione, Quanta **7**, 54 (2018).
[13] V. Gorini, A. Kossakowski, and E. C. G. Sudarshan, J. Math. Phys. **17**, 821 (1976).
[14] A. Rivas, S. F. Huelga, and M. B. Plenio, Rep. Prog. Phys. **77**, 094001 (2014).

[15] A. Rivas, S. F. Huelga, and M. B. Plenio, Phys. Rev. Lett. **105**, 050403 (2010).
[16] M. J. W. Hall, J. D. Cresser, L. Li, and E. Andersson, Phys. Rev. A **89**, 042120 (2014).
[17] H.-P. Breuer, E.-M. Laine, and J. Piilo, Phys. Rev. Lett. **103**, 210401 (2009).
[18] E.-M. Laine, J. Piilo, and H.-P. Breuer, Phys. Rev. A **81**, 062115 (2010).
[19] V. Jagadish, R. Srikanth, and F. Petruccione, Phys. Rev. A **101**, 062304 (2020).
[20] V. Jagadish, R. Srikanth, and F. Petruccione, Phys. Lett. A **384**, 126907 (2020).
[21] K. Siudzińska and D. Chruściński, J. Phys. A: Math. Theor. **53**, 375305 (2020).
[22] N. Megier, D. Chruściński, J. Piilo, and W. T. Strunz, Sci. Rep. **7**, 6379 (2017).
[23] K. Siudzińska, Phys. Rev. A **103**, 022605 (2021).
[24] V. Jagadish, R. Srikanth, and F. Petruccione, Phys. Rev. A **105**, 032422 (2022).
[25] V. Jagadish, R. Srikanth, and F. Petruccione, Phys. Rev. A **106**, 012438 (2022).
[26] V. Jagadish, R. Srikanth, and F. Petruccione, Phys. Rev. A **108**, 042202 (2023).
[27] A. Liu, D. B. Almeida, W. K. Bae, L. A. Padilha, and S. T. Cundiff, Phys. Rev. Lett. **123**, 057403 (2019).
[28] M. B. Harouni, Chin. Phys. B **29**, 124203 (2020).
[29] G. E. Fux, E. P. Butler, P. R. Eastham, B. W. Lovett, and J. Keeling, Phys. Rev. Lett. **126**, 200401 (2021).
[30] H. Zhang, B. Pokharel, E. M. Levenson-Falk, and D. Lidar, Phys. Rev. Appl. **17**, 054018 (2022).
[31] B.-W. Li, Q.-X. Mei, Y.-K. Wu, M.-L. Cai, Y. Wang, L. Yao, Z.-C. Zhou, and L.-M. Duan, Phys. Rev. Lett. **129**, 140501 (2022).
[32] C.-F. Li, G.-C. Guo, and J. Piilo, Europhys. Lett. **127**, 50001 (2019).
[33] L. B. Ho, Y. Matsuzaki, M. Matsuzaki, and Y. Kondo, New J. Phys. **21**, 093008 (2019).
[34] C. Bengs, J. Magn. Reson. **322**, 106868 (2021).
[35] V. Gulati, Arvind, and K. Dorai, Eur. Phys. J. D **76**, 194 (2022).
[36] A. Singh, H. Singh, K. Dorai, and Arvind, Phys. Rev. A **98**, 032301 (2018).
[37] H. Singh, Arvind, and K. Dorai, Phys. Rev. A **97**, 022302 (2018).
[38] A. Gautam, K. Dorai, and Arvind, Quantum Inf. Process. **21**, 329 (2022).
[39] T. Xin, S.-J. Wei, J. S. Pedernales, E. Solano, and G.-L. Long, Phys. Rev. A **96**, 062303 (2017).
[40] B. Schumacher, Phys. Rev. A **54**, 2614 (1996).
[41] I. Oliveira, R. Sarthour Jr., T. Bonagamba, E. Azevedo, and J. C. C. Freitas, *NMR Quantum Information Processing* (Elsevier, New York, 2007).
[42] D. G. Cory, M. D. Price, and T. F. Havel, Physica D **120**, 82 (1998).
[43] A. Mitra, K. Sivapriya, and A. Kumar, J. Magn. Reson. **187**, 306 (2007).
[44] N. Khaneja, T. Reiss, C. Kehlet, T. Schulte-Herbrüggen, and S. J. Glaser, J. Magn. Reson. **172**, 296 (2005).
[45] S. Dogra, A. Dorai, and K. Dorai, Int. J. Quantum Inform. **13**, 1550059 (2015).
[46] G. L. Long, H. Y. Yan, and Y. Sun, J. Opt. B: Quantum Semiclass. Opt. **3**, 376 (2001).
[47] G. M. Leskowitz and L. J. Mueller, Phys. Rev. A **69**, 052302 (2004).
[48] H. Singh, Arvind, and K. Dorai, Phys. Lett. A **380**, 3051 (2016).
[49] A. Gaikwad, K. Shende, and K. Dorai, Int. J. Quantum Inform. **19**, 2040004 (2021).
[50] A. Gaikwad, K. Shende, Arvind, and K. Dorai, Sci. Rep. **12**, 3688 (2022).
[51] D. G. Cory, M. D. Price, W. Maas, E. Knill, R. Laflamme, W. H. Zurek, T. F. Havel, and S. S. Somaroo, Phys. Rev. Lett. **81**, 2152 (1998).
[52] Y. S. Weinstein, M. A. Pravia, E. M. Fortunato, S. Lloyd, and D. G. Cory, Phys. Rev. Lett. **86**, 1889 (2001).